

Theory of Human Tetrachromatic Color Experience and Printing

JESSICA LEE, NICHOLAS JENNINGS, VARUN SRIVASTAVA, and REN NG,
University of California, Berkeley, USA

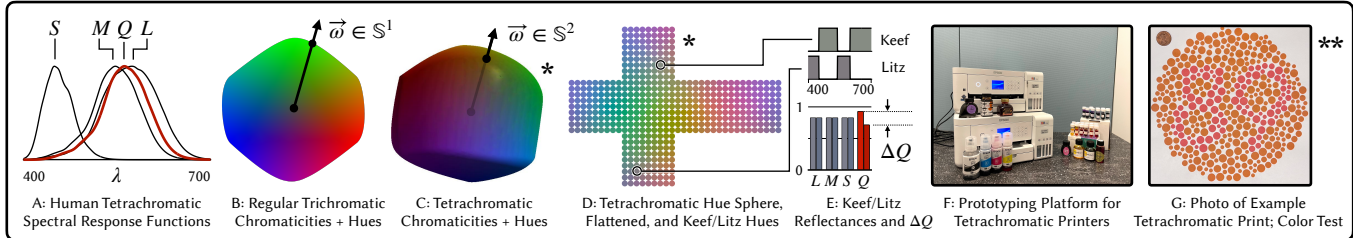


Fig. 1. We develop theory, algorithms and prototype systems for human tetrachromatic color. Tetrachromats have four types of color photoreceptors with distinct spectral response functions (A) – the conventional L , M and S cone cells, as well as a fourth Q cone. More than 50% of women are estimated to be genetic tetrachromats [Neitz and Neitz 2011]. We apply and extend generalized d -dimensional object color theory, to analytically compute all the key color structures from spectral responses (Sec. 3). In trichromacy, the result is the regular chromaticity disk (B), which is bordered by the familiar hue circle hue parameterized by $\vec{\omega} \in \mathbb{S}^1$. In a main contribution of this paper, we compute the analogous geometry for tetrachromacy, predicting a hue space (C) that is topologically equivalent to a sphere (\mathbb{S}^2). We analyze how this higher dimensional topology predicts a fundamentally richer color experience (Sec. 4) for tetrachromats. For example, the flattened cubemap of the hue sphere in (D) highlights an interesting pair of tetrachromatic hues, which we call keef and litz, that both appear gray to a trichromat but are complementary hues to a tetrachromat (as distinct as blue and yellow). An important note (*) is that the underlying colors in (C) and (D) are spectral functions, all unique to a tetrachromat, but these colors are visualized in the figure as they would appear to a trichromat – close examination shows that many unique tetrachromatic colors are confused as the same trichromatic hue. The spectral reflectance functions for colors keef and litz are shown in (E), along with their activation of the four cone cells. Note that the L , M and S cone activations are the same, hence the colors appear identical to trichromats, but the Q cone activations have a distinct ΔQ gap, enabling tetrachromats to distinguish the colors. We develop a platform for prototyping tetrachromatic color printers, using pipelined, hackable inkjet printers and a library of spectrally-characterized fountain pen inks (F). Our prototype printer achieves a four-dimensional color gamut (Fig. 10), and (G) is an example print showing a field of dots that all appear orange to trichromats, but that reveal a hidden number to a tetrachromat. The digits are faintly visible in this photograph, because the camera’s color response differs from a human’s. In person, we find that these digits are not visible to most but not all people, providing perceptual validity corroborated by spectral measurements (Sec. 5).

Genetic studies indicate that more than 50% of women are genetically tetrachromic, expressing four distinct types of color photoreceptors (cone cells) in the retina. At least one functional tetrachromat has been identified in laboratory tests. We hypothesize that there is a large latent group in the population capable of fundamentally richer color experience, but we are not yet aware of this group because of a lack of tetrachromatic colors in the visual environment. This paper develops theory and engineering practice for fabricating tetrachromatic colors and potentially identifying tetrachromatic color vision in the wild. First, we apply general d -dimensional color theory to derive and compute all the key color structures of human tetrachromacy for the first time, including its 4D space of possible object colors, 3D space of chromaticities, and yielding a predicted 2D sphere of tetrachromatic hues. We compare this predicted hue sphere to the familiar hue circle of trichromatic color, extending the theory to predict how the higher dimensional topology produces an expanded color experience for tetrachromats. Second, we derive the four reflectance functions for the ideal tetrachromatic inkset, analogous

to the well-known CMY printing basis for trichromacy. Third, we develop a method for prototyping tetrachromatic printers using a library of fountain pen inks and a multi-pass inkjet printing platform. Fourth, we generalize existing color tests – sensitive hue ordering tests and rapid isochromatic plate screening tests – to higher-dimensional vision, and prototype variants of these tests for identifying and characterizing tetrachromacy in the wild.

CCS Concepts: • Computing methodologies → Perception.

Additional Key Words and Phrases: Color, Tetrachromacy, Printing

ACM Reference Format:

Jessica Lee, Nicholas Jennings, Varun Srivastava, and Ren Ng. 2024. Theory of Human Tetrachromatic Color Experience and Printing. *ACM Trans. Graph.* 43, 4, Article 128 (July 2024), 15 pages. <https://doi.org/10.1145/3658232>

1 INTRODUCTION

We hypothesize that there is a large latent group of genetic tetrachromats in the human population who are capable of fundamentally richer, tetrachromatic color experience, but we are not yet aware of this group societally because of a lack of tetrachromatic colors in the visual environment. In this paper, we develop theory for computing and printing the spectral reflectance functions that optimally span human tetrachromatic color space, toward testing this hypothesis by attempting to produce tetrachromatic color imagery that reveals human tetrachromacy in the wild, at scale.

Authors’ address: Jessica Lee, jess.lee@berkeley.edu; Nicholas Jennings, nicholasjennings@berkeley.edu; Varun Srivastava, varun.neal@berkeley.edu; Ren Ng, ren@berkeley.edu, University of California, Berkeley, USA.

Permission to make digital or hard copies of part or all of this work for personal or classroom use is granted without fee provided that copies are not made or distributed for profit or commercial advantage and that copies bear this notice and the full citation on the first page. Copyrights for third-party components of this work must be honored. For all other uses, contact the owner/author(s).

© 2024 Copyright held by the owner/author(s).
ACM 0730-0301/2024/7-ART128
<https://doi.org/10.1145/3658232>

Conventional human trichromatic color vision is defined by the ability to distinguish three dimensions of color, formally tested by the need for three color primaries to match the appearance of any test color. Trichromacy arises from the presence of three types of photoreceptors in the retina: the short (*S*), medium (*M*) and long (*L*) wavelength cone cells. There are variations in the opsin genetic sequence associated with each cone type, giving rise to slightly different spectral sensitivity peaks [Neitz and Neitz 2011]. In a common case of color blindness, deuteranomaly, a person has two slightly different *L* cone peaks instead of one *M* and *L*.

The basis for genetic tetrachromacy is that the *M* and *L* genes are located on the X chromosome. Since women have two X chromosomes, they may inherit two distinct copies of the *M* and/or *L* genes. Genetic tetrachromacy is the case in which a woman inherits a distinct fourth cone, which we denote as the *Q* cone, with a spectral peak in between *M* and *L* (see Fig. 1A). Recent genetic studies indicate that more than 50% of women are genetically tetrachromatic [Neitz and Neitz 2011]. But so far, only one functional tetrachromat has been identified in laboratory perceptual tests [Jordan et al. 2010]. It remains an open scientific question whether functional tetrachromacy could exist at scale.

This paper develops theory and engineering practice for fabricating tetrachromatic colors and potentially identifying tetrachromatic color vision in the wild. Our first main contribution is to apply and extend general *d*-dimensional reflective color space [Koenderink 2010; Logvinenko and Levin 2022; Niall 2017] to derive and compute all the key color structures of human tetrachromacy for the first time. We compute the four-dimensional space of all material reflectances under a fixed illuminant, generally called the object color solid. Then, we derive the chromaticity space of a tetrachromat, which represents all of the unique ratios of cone stimulation, which fill a three-dimensional ball. Lastly, we derive and compute the color-circle equivalent in tetrachromatic space, predicting a sphere of maximally saturated hues called the Full Colors [Ostwald and Taylor 1931].

We analyze the theoretical implications of this predicted higher-dimensional color geometry on the perceptual experience of a tetrachromat (Sec. 4). Comparing the familiar hue circle of trichromatic color to the hue sphere, we identify that while trichromats experience each full color as being neighbored on a 1-dimensional line, tetrachromats experience each color with a full circular continuum of neighbors. As one striking example, in tetrachromacy, what a trichromat would see as orange is neighbored by a circular continuum of hues that include not only red and yellow, but also green and pink.

As our second main contribution, we theoretically derive the four reflectance functions for the ideal tetrachromatic inkset, generalizing the well-known CMY printing basis for trichromacy. We call this ideal tetrachromatic inkset CVPY, because the inks appear cyan, violet, pink and yellow to trichromats. A printer equipped with these inks would in principle be able to produce a full tetrachromatic ink gamut, including all colors on the tetrachromatic hue sphere.

As our third main contribution, we develop a method for prototyping tetrachromatic printers using a new library of spectrally-measured inks and a multi-pass inkjet printing platform. We compile a library containing not only inks similar to the cyan, magenta and

yellow inks commonly found in printers, but an additional 50 fountain pen inks that attempt to spectrally match the idealized CVPY inkset we derived. We develop an efficient optimization procedure to choose inksets from the library by estimating the color printing gamuts that result using Kubelka-Munk and Neugebauer pigment mixing math (Sec. 5.1). We show that our prototype printer is able to produce colors spanning half of the tetrachromatic hue sphere, compared to a conventional CMY printer that is limited to printing a one-dimensional line of colors on the sphere.

As our fourth main contribution, we generalize two trichromatic color tests to *d* dimensions, apply them to produce novel tests of tetrachromatic color vision, and prototype production of these tests to comprehensively evaluate the ability of our tetrachromatic printer. First, we generalize Farnsworth's FM100 color test [1943] from trichromacy to tetrachromacy, moving from ordering a 1-dimensional sampling of colors on the hue circle to ordering a 2-dimensional sampling on the tetrachromatic hue sphere. We compute and print these grids of tetrachromatic color samples (Fig. 10). Second, we generalize pseudoisochromatic plate screening tests (similar to the famous Ishihara plates [1918] for screening for conventional color blindness) to screening for *d*-dimensional color ability. We compute and print plates for the tetrachromatic case, which are unachievable by conventional CMY printers, and evaluate the results with spectral measurements and an initial perceptual study.

This paper provides a foundation for extending the color management pipeline to attempt to draw out the hypothesized tetrachromatic perceptual abilities of the latent group of genetically tetrachromatic individuals in the human population.

2 RELATED WORK

2.1 Tetrachromacy

2.1.1 Genetics of Tetrachromacy. Normal color vision is associated with expression of three distinct cone photopigments in the retina, which for a typical trichromat are the Short, Medium, and Long (*S*, *M*, *L*) cones that have spectral sensitivity peaks roughly peaking at the 420 nm, 530 nm, and 559 nm wavelengths. The *M* and *L* cone opsin genes, OPN1MW and OPN1LW, lie on the X chromosome, which is sex-linked. Men inherit one copy of the X chromosome, and women inherit two. Genetic recombination of X-chromosomes has evolutionarily resulted in a number of different, spectrally-shifted copies of the *M* and *L* genes [Neitz and Neitz 2011].

A woman is genetically tetrachromatic if her two X chromosomes contain three genetically distinct variants of the *M* and *L* genes (resulting in a total of four with the *S* gene, on chromosome 7). Indeed, Neitz and Neitz estimate from genetic sampling studies that “more than half” of women are genetically tetrachromatic [Davidoff 2015; Neitz and Neitz 2011; Neitz et al. 1993].

2.1.2 Functional Tetrachromacy. Jordan et al. [2010] show that functional human tetrachromacy exists, identifying a subject (cDa29) as such through detailed laboratory perceptual tests. The genotype possessed by cDa29 is rare, with an estimated prevalence of approximately 1% of women [Davidoff 2015], but it may be the most likely genotype to be functional (with a *Q* cone spectral peak that is 12 nm from *L*, close to the midpoint between *M* and *L*). In contrast, the most common tetrachromatic genotype (“ser180ala heterozygous”)

has an estimated prevalence of 47% of women [Jordan and Mollon 2019], but has a smaller 4–5 nm gap between Q and L . One could postulate that such a gap between Q and L is too small to be functional, and indeed no functional tetrachromats with this genotype have yet been identified; however, a smaller gap of 2 nm has been shown to be sufficient to add a functional dimension of color in an anomalous trichromat male [Davidoff et al. 2016].

This evidence leads to the possibility that latent functional tetrachromacy exists in the population at scale, but we are societally unaware of it because of a lack of tetrachromatic colors in the visual environment. Evidence of such lacking is provided by Wachtler et al. [2007] and Rezeanu et al. [2021].

2.1.3 Modeling Tetrachromatic Vision. The geometric consequences of the dimensional increase in the color space for human tetrachromats have yet to be fully explored. Central to our work is the idea of an object color solid, which is the set of all possible spectral reflectances under a given white-point for an d -dimensional observer. Applying such theory, Koenderink posits that tetrachromats have a 2D hue sphere, and that tetrachromats should have a qualitatively different experience of the colors of the rainbow compared to trichromats [2010]. Hummingbirds, which are genetic tetrachromats with an additional cone sensitive to UV light, are able to detect and differentiate non-spectral colors [Stoddard et al. 2020]. Hummingbird researchers have modeled these non-spectral colors as the lines connecting points on a tetrahedra [Burkhardt 1989; Goldsmith 1990] and utilized them to study evolutionary bird reflectances [Cooney et al. 2022; Stoddard and Prum 2008; Venable et al. 2022], but characterizing the full topology of tetrachromatic colors has yet to be explored, which we contribute in this work.

2.2 Object Color Theory

2.2.1 Characterizing the object color solid. Schrödinger [1920] first defined the concept of optimal object colors, which are colors that are the most luminous for each chromaticity. He theorized a one-to-one relationship between the optimal object colors and a class of reflectance functions called the two-transition functions [Niall 2017]. Two-transition functions are indicator functions $\mathbb{R} \rightarrow \{0, 1\}$ that flip between $0 \rightarrow 1$ or $1 \rightarrow 0$ at two wavelengths. In order to prove Schrödinger’s claim with more mathematical rigor, MacAdam [1935] used a center-of-mass argument to show that two-transitions should always be further apart in the chromaticity diagram than any other pair of reflectances. West and Brill [1983] stated that a spectral locus must be convex and well-ordered in wavelength to abide by Schrödinger’s formulation of optimal colors, demonstrating for bumblebee cones, the optimal object color theorem does not hold due to their non-convex spectral locus.

Centore [2013] took a geometric approach to finding optimal colors by relating the boundary of a zonohedron to the optimal object colors. Logvinenko and Levin [2022] extended color geometry to the d -dimensional continuous case, and even posited conditions for all optimal object colors to have $d - 1$ transitions, which they call the Schrödinger-Maximov condition. We compute the optimal object color solid for a tetrachromat for the first time.

2.2.2 Full Colors. Ostwald was interested in an analogous but different problem than Schrödinger: what spectrum gives the most saturated color for every hue? In other words, what physical pigments give rise to the color circle? His experiments found that a reflectance that reflected about half of a contiguous part of the spectrum would be the most saturated spectrum at a certain hue, which he called a *Full Color* [Ostwald and Taylor 1931]. Koenderink et al. [2021] noted that the Full Colors are the furthest points from the achromatic axis per hue in the object color solid, computing them by taking the convex hull of points projected along the luminance axis. An equivalent approach to finding Full Colors is finding the point whose tangent hyperplane is parallel to the achromatic axis, which Logvinenko and Levin solve by linear programming [2022]. In Section 3.3, we extend the approach of Koenderink et al. to compute the Full Colors of d -dimensional observers for the first time.

2.3 Inkjet Printing

To produce a given color with a set of k ink primaries, printers will cover a given area with a certain percentage of each ink channel using random halftoning techniques. When viewed from a sufficient distance, these halftone microdots visually blend to form the desired color. The Neugebauer equations provide a simple probabilistic model which can predict the spectra of a mixture of inks at arbitrary percentages, given a complete measurement of ink *superpositions*, e.g. the spectra of inks printed directly on top of each other. A basis of k ink primaries will have 2^k superpositions, corresponding to all binary combinations of the primaries.

For a large catalog of inks, measuring all 2^k Neugebauer superpositions to simulate the ink gamut is often intractable. In the best case, we would like to measure only our K -ink library of reflectances. Several approaches via neural networks have been tried, either via predicting the mixture of reflectances directly, or by translating reflectances into a form that can be solved with mixed integer linear programming [Ansari et al. 2020; Shi et al. 2018]. The Kubelka-Munk (KM) equations provide a simple model for mixing pigments [Kubelka 1931; Sochorová and Jamriška 2021], and have been used to simulate the Neugebauer superpositions [Shi et al. 2018; Wei et al. 2011]. While many of the physical properties of paint-mixing don’t fully translate to the domain of printer inks, KM simulations provide a reasonable approximation for our purposes.

In order to select the best set of k primaries from a K ink library, we must have a way to compare different sets of inks. Stollnitz et. al. describe a method for modeling the gamut of a given set of inks, recreating a given image, and comparing its colors in $L^*a^*b^*$ space to the target image. This comparison is used to score sets of inks, and an optimal ink basis can be generated using a genetic algorithm [Stollnitz et al. 1998]. Shi et. al. developed a similar approach, using both $L^*a^*b^*$ coordinates and full-spectral predictions to compare the results from their large-scale 3D printing system to the colors of target paints. Their printing gamut included typical CMYK inks, as well as an additional 7 inks chosen for their similarity to commonly used paints [Shi et al. 2018]. Beyond academic studies, several internet communities exist dedicated to cataloging inks and tackling custom ink printing. The website Mountain of Inks contains a massive catalog of commercial fountain pen inks including

photographs along with measurements of physical properties such as dry time, sheen, and water resistance [McCown 2023].

Beyond spectral reproduction, several works have attempted to fabricate reflectors that display different images based on view angle [Sakurai et al. 2018], print hidden images inside of specular reflectances [Pjanic and Hersch 2015], or by programmatically changing dyes [Jin et al. 2020]. In this paper, we focus on printing reflectances that look distinct to tetrachromatic observers, but are metameric and appear the same to a trichromatic observer, printing the hidden image in an Ishihara-like test.

2.4 Color Vision Tests

Color vision tests attempt to discriminate observers into classes of color deficiency, based on the properties of their color space. The most comprehensive test for color vision is known as the Farnsworth-Munsell test, which discriminates trichromatic observers from dichromatic observers based on their performance on ordering a total of 100 equiluminant and equisaturated tiles into a circle [Farnsworth 1943]. A dichromatic observer will have a line of confusion depending on the missing cone, and will place colors incorrectly across the line, whereas a trichromat will not be confused. We generalize the construction of this test to d -dimensions.

One can also test across a specific confusion line, which is most commonly known as an Ishihara test [1918], shown to effectively detect protanomaly and deutanomaly [Birch 1997]. Ishihara tests works by showing the subject a series of image (also called plates) formed by dots colored with different pairs of colors that lie along a confusion line. They contain a hidden image drawn with metamerically colored dots, so that observers who can't distinguish the colors will only see a uniform image of dots. A level of artificial luminance noise is added to the dot colors. This helps to ensure that the only way to pass the test is through noticing chromatic differences in the colors [Souza et al. 2014]. By assessing which, if any, plates a subject fails to see the hidden image in, the general type of color blindness of a subject can be determined. We generalize the construction of an Ishihara test for an arbitrary set of cones.

An anomaloscope is an color matching instrument that displays a bipartite half field. Typically, one half is a monochromatic yellow-orange test light, and the second half field is an adjustable mixture of red and green monochromatic lights. Subjects adjust the ratio of the mixture light until they see it visibly match the test color. The test can be used to predict what spectral peaks a subject has for the M and L cones and is used for identifying anomalous trichromats [Barbur et al. 2008]. Jordan et al. [2010] used the anomaloscope to functionally test for tetrachromatic vision. Since the spectral locus curves in 3D chromaticity space, a tetrachromat will always be able to distinguish the spectral color of the target light from the non spectral color of the mixture light, and will never find a ratio that matches the target [Jordan et al. 2010].

3 OBJECT COLOR THEORY IN d -DIMENSIONS

The following d -dimensional color solid geometry are visualized comprehensively for the mono-, di-, tri- and tetrachromatic cases in Figure 2. We use the Stockman and Sharpe cone fundamentals for L , M and S spectral response functions [Stockman and Sharpe 2000;

d	Color dimensionality of vision; number of cone photoreceptor types (see 2.1).
L, M, S, Q	Spectral response functions respectively for long, medium, short and 4th human cone cells (see 2.1).
λ	Wavelength, usually restricted to a subset of the visible light spectrum $\Lambda \subset \mathbb{R}$.
S_1, \dots, S_d	Spectral response functions for d cone cells in general d -dimensional color vision.
\mathcal{L}	Spectral locus curve for d -dimensional color vision (see eq. 1).
R	An object reflectance function $\Lambda \rightarrow [0, 1]$, mapping each wavelength λ to a percentage of light reflected back.
$\vec{S}(R)$	The color of a reflectance R as perceived by the d -dimensional observer, called an object color (see eq. 2).
O	The object color solid, or set of all object colors (see eq. 3).
$\Omega_1, \dots, \Omega_d$	Max basis vectors (see 3.2).
\mathcal{P}	The parallelotope induced by the max basis vectors (see 3.2).
Π_1, \dots, Π_d	Printing primary basis vectors for object color solid (see 3.2).
$(\vec{\omega}, s)$	Chromaticity coordinates for a d -dimensional color observer, represented in polar coordinates with generalized hue angle $\vec{\omega} \in \mathbb{S}^{d-2}$ and scalar saturation, s .
G_1, G_2, \dots, G_{d-1}	A basis for the chromaticity space \mathbb{R}^{d-1} in Cartesian coordinates for a d -dimensional observer.

Table 1. Glossary

Stockman et al. 1999]. We model the Q cone peak at 545 nm [Jordan et al. 2010] to match the functional tetrachromat cDa29 by shifting the M cone fundamental. We pick the CIE standard illuminant D65 for our computations [CIE 2004]. We note that the output of the following algorithms in the section are dependent on the choice of cone fundamentals, peaks, and illuminant.

3.1 Object Color Solid

The object color solid O is the set of all possible perceivable colors of material objects. The solid is d -dimensional, existing in the latent space of the d -dimensional observer. The maximal point of the solid, usually normalized to $\vec{1} = (1, 1, \dots, 1)$, represents reflecting back the entirety of the illuminant, and it is called the whitepoint. Correspondingly, the origin $\vec{0} = (0, 0, \dots, 0)$ can be called black. The object color solid is often referred to as the reflectance gamut [Niall 2017] of the d -dimensional observer, and is the latent space where all colors, chromaticities, and hues can be precisely identified.

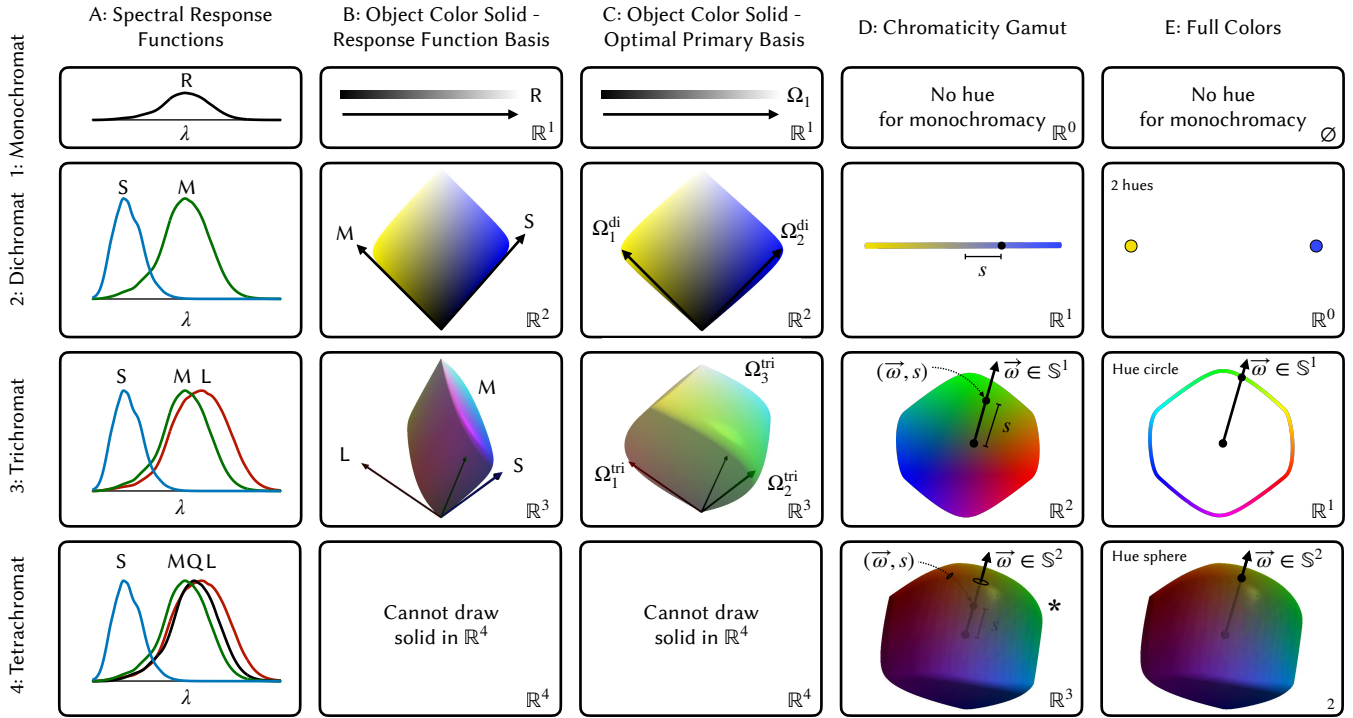


Fig. 2. Key Geometrical Structures for d -Dimensional Color Vision. Computed and visualized here for $d = 1, 2, 3, 4$ corresponding to mono-, di-, tri and tetrachromatic vision. Column A shows the spectral response functions for the assumed d cone photoreceptor cells; in A4, the Q function in black is the 4th cone response function for genetically tetrachromatric females. Column B plots the object color solid in the response function basis, and column C plots the same in the Optimal Primary Basis. B3 and C3 show the importance of the Optimal Primary Basis for plotting the solid as isotropically as possible — this is even more important in the tetrachromatic case, although the solid cannot be drawn in B4 and C4 since it is four dimensional. Column D plots the chromaticities, projecting out the luminance dimension, decreasing the dimension by 1 as shown; the results for di-, tri- and tetrachromacy, respectively, are a 1D chromaticity line (cell D2), 2D chromaticity disk (D3), and 3D chromaticity ball (D4). The chromaticity is parameterized by coordinates $(\vec{\omega}, s)$, where $\vec{\omega} \in \mathbb{S}^{d-2}$ is a unit-length vector parameterizing a hue by a direction and scalar s is the saturation of the color. For example, cell D3 shows the familiar case of trichromacy, where the chromaticity shown corresponds to a direction $\vec{\omega}$ pointing towards a green hue, and s represents a mid-saturation level. Finally, Column E shows the Full Colors, which are the colors corresponding to maximum saturation for each hue direction; E2 shows the zero dimensional hue space for dichromacy (yellow and blue hues only, in this case for protanopia), and E3 shows the familiar 1D hue circle (all colors of the rainbow and purple) for trichromacy. Finally, E4 shows one of the major novel contributions of this paper, the first computation of the predicted 2D hue sphere for tetrachromacy. A crucial comment (*) for the tetrachromatic chromaticities (4.D) and Full Colors (4.E) is that these are drawn in the colors that they would appear to a trichromat, because we cannot display tetrachromatic colors in conventional colormaps and file formats.

Consider a d -observer with cone sensitivities S_1, \dots, S_d over a range of light frequencies $\lambda \in \Lambda \subset \mathbb{R}$. The *spectral locus* is the 1-dimensional curve of colors

$$\{S_1(\lambda), \dots, S_d(\lambda) \in \mathbb{R}^d \mid \lambda \in \Lambda\} =: \mathcal{L}(\lambda) \subset \mathbb{R}^d. \quad (1)$$

We note that this curve is associated with the continuum of monochromatic (single-wavelength) colors.

An object reflectance $R(\lambda) \in \mathbb{L}^\infty$ is a function $\Lambda \rightarrow [0, 1]$, mapping each wavelength to a percentage of light reflected back. The observed color $\vec{S}(R)$ under some illuminant $I \in \mathbb{L}^\infty$ is

$$\left(\int_\Lambda S_1(\lambda)I(\lambda)R(\lambda)d\lambda, \dots, \int_\Lambda S_d(\lambda)I(\lambda)R(\lambda)d\lambda \right) \in \mathbb{R}^d. \quad (2)$$

We additionally normalize each component i by $\int_\Lambda S_i(\lambda)I(\lambda)d\lambda$ so that the whitepoint of the gamut is $\vec{1}$.

This projection $\vec{S} : \mathbb{L}^\infty \rightarrow \mathbb{R}^d$ is verifiably a linear map. It follows that this projection is of full rank if and only if the cone mechanisms S_i are linearly independent. We therefore assume a d -dimensional observer must have linearly independent cone mechanisms.

The object color solid is defined as the set

$$\mathcal{O} := \{\vec{S}(R) \mid R \in \mathbb{L}^\infty, 0 \leq R(\lambda) \leq 1\} \subset \mathbb{R}^d. \quad (3)$$

Since \vec{S} is a linear projection $\mathbb{L}^\infty \rightarrow \mathbb{R}^d$, we see that \mathcal{O} is a projection of the set of reflectances. Since the latter is evidently convex in \mathbb{L}^∞ , \mathcal{O} must also be convex in \mathbb{R}^d . It therefore suffices to simply calculate the points on the boundary of the object color solid in order to determine all object colors.

The colors on the boundary of the object color solid have historically been called *optimal colors*, since they correspond to the points of greatest magnitude, or luminance, on the object color solid

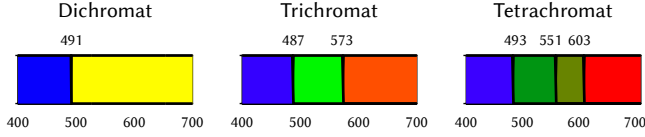


Fig. 3. Computed Optimal Primary Bases for Di-, Tri- and Tetrachromats. The graphs show the optimized 2-, 3- and 4-partitions of white for each case (see 3.2). Note the trichromatic case splits white into Red, Green, and Blue.

for a given chromaticity. We direct the reader to the related works section for a detailed history of the computation of the boundary of the object color solid.

Here, we refer to Logvinenko and Levin [2022] who prove that any point on the boundary of O is associated with a $d-1$ -hyperplane that intersects the spectral locus. We restate their theorem:

THEOREM 3.1 (LOGVINENKO AND LEVIN). *For a nonzero vector $H \in \mathbb{R}^d$, define a reflectance function R_H such that*

$$R_H(\lambda) := \begin{cases} 1 & H \cdot \mathcal{L}(\lambda) > 0, \\ 0 & H \cdot \mathcal{L}(\lambda) < 0. \end{cases}$$

A point is on the boundary of the object color solid O if and only if it is of the form $\vec{S}(R_H)$ for some H .

We refer the reader to the text for foundational lemmas toward the proof of this theorem. We note that H is defining a halfplane $H \cdot x = 0$ that is splitting the spectral locus into two halves. The wavelengths of the intersections $\lambda_1, \dots, \lambda_m$ on the spectral locus define the values on which R_H switches between 0 and 1. In general, such a reflectance that switches between 0 and 1 at m locations is called an m -transition function.

This theorem allows us to generate the boundary of the object color solid by sampling halfplanes in \mathbb{R}^d , computing the corresponding transition function, and measuring the stimulus $\vec{S}(R_H)$. Logvinenko and Levin [2022] suggest sampling halfplanes by picking vectors in the unit sphere and taking their tangent. However, as we simulate higher dimensions, picking a uniform grid to sample a hypersphere must be done stochastically, which does not trivially induce a mesh. Instead, we propose an improvement by directly sampling all of the halfplanes that intersect the spectral locus up to a discrete stepsize [Eppstein 1995]. This technique solves the curse of dimensionality associated with sampling from a hypersphere, and ensures we consistently sample the spectral locus. Additionally, cone data acquired via color-matching is often specified at discrete wavelengths, for example 390nm, 391nm, ..., 700nm, rather than as a continuous function. This induces an inherent quantization on the spectral locus, which we can use directly rather than relying on a continuous interpolation. As a result of sampling the spectral locus, the method recovers $d-1$ -dimensional facets for every point generated on the boundary, creating a water-tight mesh. We show the complete object color solid O for various dimensions in Figure 2B.

3.2 The Max Basis Ω

The ambient space of the object color solid is currently in the basis given by the activation sensitivities of the d -dimensional observer

(Figure 2B). Following the work of Koenderink et al. [2021] for the trichromatic case, we find a linearly isomorphic basis for the space that maximizes the volume of the object color solid. This procedure will naturally decorrelate the axes, rounding the shape of the gamut. This will aid in visualization (Figure 2C) and will prove to be an advantageous coordinate system for analyzing the gamut.

A d -partition is a partition of the visible wavelengths into d parts. Formally, d parts are created from $d-1$ cutpoints $\lambda_1, \dots, \lambda_{d-1}$, with indicator functions $\mathbb{1}_{a \leq \lambda < b}(\lambda) := \{1 \text{ if } a \leq \lambda < b, 0 \text{ otherwise}\}$, and d -partition with respect to illuminant I defined as:

$$\text{Part}(\lambda_1, \dots, \lambda_{d-1}) := \{I \mathbb{1}_{\lambda_{min} \leq \lambda < \lambda_1}, I \mathbb{1}_{\lambda_1 \leq \lambda < \lambda_2}, \dots, I \mathbb{1}_{\lambda_{d-1} \leq \lambda \leq \lambda_{max}}\} \quad (4)$$

We define vectors p_1, \dots, p_d by projecting the partition $\text{Part}(\lambda_1, \dots, \lambda_{d-1})$ into the cone response basis \vec{S} , that is,

$$(p_1, \dots, p_d) := \mathcal{L} \cdot \text{Part}(\lambda_1, \dots, \lambda_{d-1}).$$

Consider the parallelotope \mathcal{P} that is generated from the Minkowski Sum of (p_1, \dots, p_d) ,

$$\mathcal{P}(p_1, \dots, p_d) := \{b_1 p_1 + \dots + b_d p_d \mid b_i \in [0, 1]\}.$$

The parallelotope creates a lattice with 2^d vertices that represent all of the discrete combinations of the vectors (p_1, \dots, p_d) . We can label the vertices of this lattice according to binary sequences, e.g. so that the bit sequence (b_1, \dots, b_d) represents $b_1 p_1 + \dots + b_d p_d$. Under this condition, all of the points in $\mathcal{P}(p_1, \dots, p_d)$ always lie within the object color solid O since black, white, and the d -partition vectors lie inside the solid.

Considering the set of all d -partitions, we follow Koenderink et al by choosing the parallelotope with maximal volume. The volume can be computed as the determinant of the vectors (p_1, \dots, p_d) . We compute the solution of the following optimization using brute force on a discretization of the wavelengths:

$$\lambda_1^*, \dots, \lambda_{d-1}^* := \underset{\lambda_1, \dots, \lambda_{d-1}}{\arg \max} (\det(\mathcal{L} \cdot \text{Part}(\lambda_1, \dots, \lambda_{d-1}))). \quad (5)$$

We call $\Omega_1, \dots, \Omega_d := \mathcal{L} \cdot \text{Part}(\lambda_1^*, \dots, \lambda_{d-1}^*)$ the maximal basis for the object color solid. We show the results of our maximal basis cutpoints and associated primaries for the di-, tri- and tetra- cases in Figure 3, and the object color solid visualized in the Ω basis in Figure 2C.

We also define the dual of the optimal basis primaries, $\Pi_1, \dots, \Pi_d := \vec{1} - \Omega_1, \dots, \vec{1} - \Omega_d$. These are the *opponent colors* for every max basis primary vector. We show in Section 5.1 that this creates the optimal printing ink basis.

3.3 Theory of Full Colors

In this paper, we make a critical assumption that color space expands in hue dimension as d increases, generalizing Koenderink [2010] who posited a hue sphere for tetrachromacy, and consistent with Logvinenko and Levin's concept [2022] of the $d-2$ dimensional equator in colorspace.

These concepts generalize the old idea of the color circle as the representative manifold of the most saturated colors for a trichromat, which Ostwald called the Full Colors [Ostwald and Taylor 1931]. We generalize to d -dimensional color, defining the Full Colors as the $d-2$ dimensional manifold of all maximally saturated colors. Given a

hue direction $\vec{\omega} \in \mathbb{S}^{d-2}$, there is a 2-dimensional plane of colors that have the same hue, but vary in luminance and saturation. The point with the largest saturation value on the plane is the full color for that hue. A sample of these cross-sections are shown in Figure 4 for the di-, tri-, and tetrachromatic cases. Since the object color solid is convex, there is always a unique furthest point. Mathematically, full colors are points on the object color solid whose tangent hyperplane is parallel to the luminance vector, noted by Logivenko and Levin [2022].

3.3.1 Computing the Full Colors. We compute the Full Color manifold from the object color solid in the Ω basis. First, we want to project away the achromatic axis, or the line from $\vec{0}$ to $\vec{1}$. Equivalently, this line is the luminance axis of the object color solid. Practically, we rotate and reflect the object color solid in the Ω basis such that this axis becomes a basis vector. We compute this transform by deriving a generalization of what Koenderink et al. call the Hering matrix $\mathcal{H}^{d \times d}$. In particular, the first row of \mathcal{H} is the equally weighted sum of all components, or the normalized unit vector $\frac{1}{\sqrt{d}}\vec{1}$. We set the remaining rows to be orthonormal axes, which we generate using finite difference coefficients, where the i th row is the finite difference of order i [Taylor 2016]. We drop the first component via a projection matrix $\text{Proj} : \mathbb{R}^d \rightarrow \mathbb{R}^{d-1}$. The linear basis of this projected space is $\Omega\mathcal{H}_2, \Omega\mathcal{H}_3, \dots, \Omega\mathcal{H}_d =: G_1, G_2, \dots, G_{d-1}$, where \mathcal{H}_i represents the i th row of the Hering matrix. Next, we can drop the first component via a projection Proj_1 . This retrieves the chromaticity solid,

$$G := \text{Proj}_1\{(\mathcal{H}\Omega v) \mid \forall v \in \mathcal{O}\}. \quad (6)$$

The set of hues can finally be computed as the convex hull of the chromaticity solid, $\text{conv}(G)$. We show the chromaticity and full colors manifold at various dimensions in Figure 2E.

3.4 Color Lattice Underlying the $d - 2$ -dimensional Hue Manifold

What are the landmarks, or the most important colors of note on the full colors manifold? In the trichromatic case, there are a finite number of unique colors that one would identify on the color circle. Following the work of Koenderink et al. [2021], we will generalize the notion of RGB and CMY as primary colors on the color circle. We identify these colors on the vertices of the max basis parallelotope \mathcal{P} , whose vertices correspond to bit sequences in Ω . We plot the vertices and edges of the projected parallelotope and its corresponding reflectances in Figure 5 for the tri- and tetrachromatic case. We can move through the parallelotope by adding or subtracting each of the basis vectors, which means every vertex has d neighbors. In total, there will be $\frac{d}{2} \times 2^d$ edges. In the projected space of chromaticities, we refer to these vertices and edges as the *hue lattice*. There are $2^d - 2$ vertices in the lattice, since the white and black points are projected away. The number of total edges in the lattice is $\frac{d}{2} \times 2^d - 2d$, since we remove all edges connecting to the white and black points.

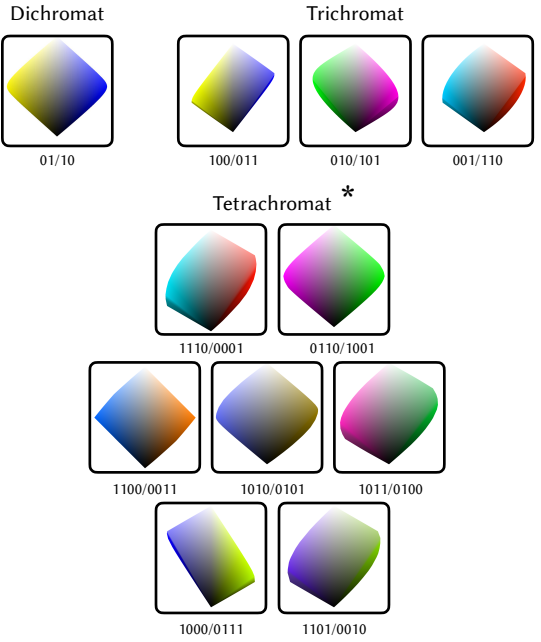


Fig. 4. Complementary Hue Slices of the Object Color Solid. These are also known as Ostwald slices. Within the d -dimensional object color solid, for every hue vector $\vec{\omega} \in \mathbb{S}^{d-2}$, there exists a slice of the color solid containing all the colors of associated hue and its complementary hue $-\vec{\omega}$. The colors in the slice vary over all luminance and saturation. The saturation achieves a maximum possible value for each hue at a specific luminance that is the complementary luminance to its complementary hue, as shown in each slice of the figure. The figure shows the slices for the cardinal hue directions for di-, tri- and tetrachromacy, specified via the opposing vertices of the parallelotope \mathcal{P} .

3.5 $d - 1$ dimensional Color Blindness

Color blindness arises when we compare the color experiences between a $d - 1$ and a d -dimensional observer. Assuming the latter has a set of cones S_1, \dots, S_d and the $d - 1$ -dim observer is missing the S_i cone, the line of confusion lies in the direction of the basis vector S_i in the response function space. This direction is commonly called the confusion line. If you consider the line of this direction that intersects the origin in the chromaticity space of the d -dimensional observer, it will intersect the boundary the solid at exactly two points that will appear completely *achromatic* and metamerically to a $d - 1$ -dimensional observer, but maximally saturated and distinct to a d -dimensional observer. In the human tetrachromatic case, normal trichromats are color blind along the Q direction. We name the associated achromatic points *keef* and *litz* (see Figure 11).

3.6 Generalized Perceptual Tests of Color Dimensionality

With this framework of computing the color spaces of arbitrary d -dimensional observers, we can generalize color tests with respect to a particular observer with cone fundamentals $\vec{R}(\lambda)$. The purpose of the test is to identify the dimensionality of the observer, and here

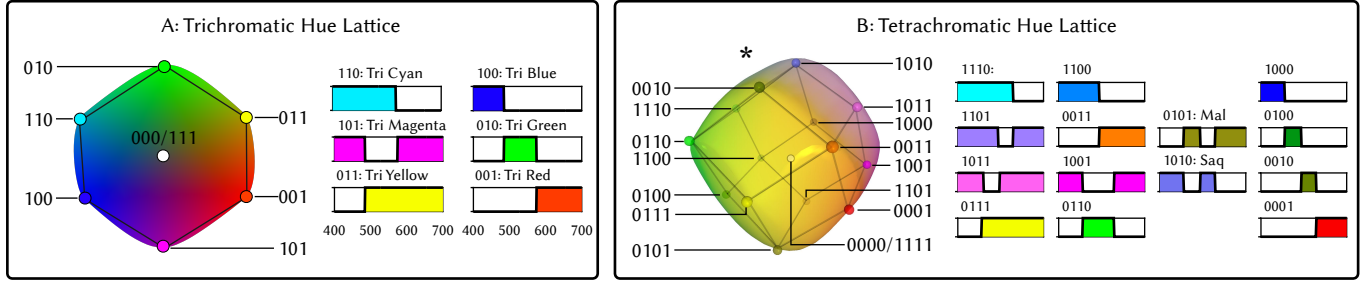


Fig. 5. Examples of Color Lattice Underlying Trichromatic Hue Circle and Tetrachromatic Hue Sphere. As described in Section 3.4, there is a discrete lattice underlying the hue manifold for d -dimensional color, comprising the 2^d additive combinatorial possibilities of the d Max Basis Ω reflectance functions, of which 2 are the achromatic colors white and black, and the remaining $2^d - 2$ are the cardinal hues. For example, Box A shows that the lattice for the trichromatic hue circle is a hexagon; and Box B shows that the lattice for the tetrachromatic hue sphere is a polyhedron with 14 vertexes. In this figure, the bit sequence associated with each vertex gives the combinations of the Max Basis vectors that form the reflectance function underlying that vertex's color. The reflectance functions are graphed as a function of wavelength over the visible spectrum from 400 to 700 nm. For example, bit sequences 100 and 010 are the Max Basis reflectances for trichromatic blue and green, respectively, and 110 represents the addition of the two reflectance functions to get cyan as shown. Notice that the edges in the lattice connect vertexes with bit sequences that differ by exactly one digit. When the dimension is increased, one maximally different pair of $d - 1$ transition reflectance functions arises. In the trichromatic case these are 010 and 101 (green and magenta) and in the tetrachromat case they are the three-dimensional transition functions 1010 and 0101, named respectively *Saq* and *Mal* (named for *SQ* and *ML*). These reflectances tend to look desaturated to a lower-dimensional observer since they tend to stimulate each cone non-optimally.

we design a test to discriminate color observers between $d - 1$ and d observers.

3.6.1 Generalized Hue Ordering Tests for d -Dim Color Observers. The most comprehensive benchmark for testing one's ability for discriminating trichromatic colors is a hue ordering test known as the Farnsworth-Munsell 100 (FM100) [Farnsworth 1943]. Subjects are tasked to order colored chips that evenly sample the hues in the trichromatic color circle. A trichomat sees each of the hues on the chips as a distinct color, and so should be able to order the hues without much difficulty. A dichromat, however, would experience some of the hues as metamers and would not be able to distinguish them. As a result, they are very likely to place the hues in the wrong order.

We theoretically generalize the procedure of creating a hue ordering test for d -dimensional observers. We first sample a hue $d - 1$ -sphere with radius s inside of the chromaticity space, where s corresponds to the saturation. Then, we pick a luminance value l for each point, to create an equiluminant and equisaturated hue ordering test. An observer with $d - 1$ dimensions that is missing cone S_i will be confused along the axis that corresponds to a change in S_i , but no change in the rest of the cones. A d -dim observer will have little trouble distinguishing the colors along each of the d axis because each side of the line corresponds to a perceptually opponent color. Therefore, passing an organization test identifies a d -dim observer.

3.6.2 Generalized Screening Tests for d -Dim Color Observers. Cambridge color tests [Reffin et al. 1991] and Ishihara plates [1918] rapidly screen possible color anomalous individuals by testing their color discrimination along a specified confusion line, corresponding to the axis of the missing cone S_i . More generally, these tests are called pseudoisochromatic plates. They ask observers to distinguish chromaticities in a field of varying luminance noise, which is known

to be functionally similar to color discrimination in nature [Regan et al. 1994].

In particular, if we want to know if an observer has the S_i cone, we can choose a pair of stimuli that differ in the activation of S_i , but remains constant in the remaining cones. This is commonly known as a confusion color pair. We call the remaining cones $\{S_1, \dots, S_d\} \setminus \{S_i\}$ the *metamer set*. Therefore, for this population, you can create d tests for each cone you want to identify. An observer who can pass all d of these tests would be considered to have d cones. In practice, people have differing spectral sensitivity peaks depending on their genetics [Neitz and Neitz 2011], not a binary set, so constructing a set of d pseudoisochromatic plates to identify d -dimensional observers would not be comprehensive, as observers who don't match the chosen metamer sets may be able to pass the test even though they don't have d cones.

To construct a plate, we first find a confusion color pair for a given set of cones. We then generate a image populated with random dots of varying sizes, and color these dots using the confusion colors to create a hidden image. Noise is added to the luminance of the color of each dot to help ensure observers are spotting chromatic differences in the dots and not imperfections in the print. If a subject is able to see the hidden image, this indicates that they must have at least one cone outside the metamer set for the plate. Subjects that can't see the hidden image must only have cones with activation functions similar to cones in the metamer set.

4 THEORY OF TETRACHROMATIC COLOR EXPERIENCE

What do these theoretical models say about the actual perceptual experience of a human tetrachromat? The higher dimensional topology of the tetrachromat hue sphere creates a fundamentally different, and in many ways richer color experience compared to trichromacy. Here, we predict several features of this higher dimensional color experience under the assumptions that color expands in the hue

dimension, as described in Section 3.3. The named colors in this section are those perceived by a trichromat with the chosen cone fundamentals and illuminant described in Section 3.

4.1 No Natural Tetrachromatic Analogue of the Rainbow

A rainbow is a natural optical phenomenon that delights trichromatic vision, because it displays a near-complete set of hues (except purple), in maximum saturation, and in the visually-pleasing order defined by the hue circle. However, a natural rainbow could not delight tetrachromatic vision in the same way, because it would display only a limited subset of tetrachromatic hues, limited to a 1-dimensional arc on the 2-dimensional hue sphere. While a trichromat or dichromat might associate rainbows with "all colors", a tetrachromatic observer would make no such comparison. The analogue to the rainbow for a tetrachromat would be an optical phenomenon occupying a 2D area of the visual field, and presenting all possible hues in maximum saturation and in the natural 2D neighbor relationships revealed by the mathematics of the hue sphere. It seems that no natural phenomenon would produce such an effect.

However, this analogue of the rainbow can certainly be produced using the methods derived in this paper. For example, the ideal variation in reflectance functions over area is defined in Fig. 9, and displayed as a flattened cubemap in Fig. 10. Indeed, Fig. 10C is a prototype physical print that represents the first physical manifestation of the tetrachromatic rainbow. This example of the rainbow underscores the crucial role that color reproduction technology would need to play if the full breadth of tetrachromatic color experience were to emerge.

4.2 Every Tetrachromatic Hue is Ringed By Its Own Unique Hue Circle

Another fundamental difference in color experience for trichromats and tetrachromats is due to the neighbor relationships between hues. In trichromacy, every hue has exactly two neighbors – this is fundamentally due to the topology of the hue circle, where every point on the line has two neighboring points. In trichromacy, orange is bordered by yellow and red, certainly not green or pink.

Remarkably, this exact neighboring relationship is turned on its head in tetrachromacy. Looking at Figure 6, we investigate the neighbors of what appears to be an orange color to trichromats, or more precisely the reflectance that reflects all light at wavelengths longer than 551 nm. The figure illustrates that if a trichromat saw a tetrachromat perform the hue ordering test, they would see orange ordered next to not only red and yellow, but also green and pink. These notable tetrachromatic neighbors can be identified in the lattice described in Section 3.4 and drawn in Fig. 5. More generally, every hue for a tetrachromat exists on the sphere and is therefore ringed by a unique circle of tetrachromat hues, and the notable tetrachromatic neighbors can be read off the cycle of neighboring vertexes in the lattice.

4.3 Tetrachromats are Surrounded by Color Blindness

One of the earliest tells that a child is color blind occurs during art class. Since hues like green and pink are confused in red-green color blindness, a color blind child often paints the grass pink, and a rose

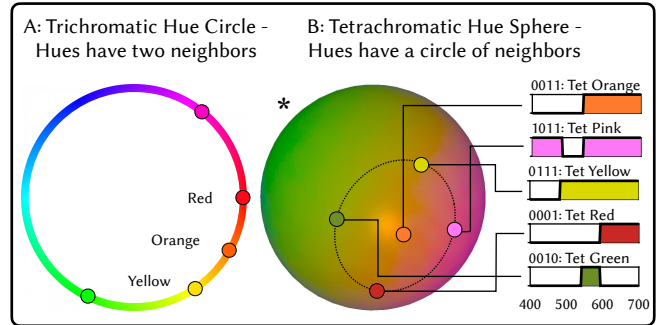


Fig. 6. Every Tetrachromatic Hue has a Circular Continuum of Neighboring Hues. A: first, for comparison, observe that in regular color vision, every hue has exactly two neighbors because of the topology of the hue circle. For example, orange's neighbors are red and yellow, but not pink or green. B: the situation is different in tetrachromatic color experience: orange neighbors pink, yellow, green and red. Keep in mind (*) that the tetrachromatic hues on the sphere are visualized as they would appear to a trichromat, but to a tetrachromat, all neighboring hues would be equally similar in their color relationship to orange. Spectral reflectance functions are shown for these five colors. This example illustrates that every tetrachromatic hue possesses a circle of neighboring hues. The topology of tetrachromatic color experience is fundamentally different than regular trichromacy.

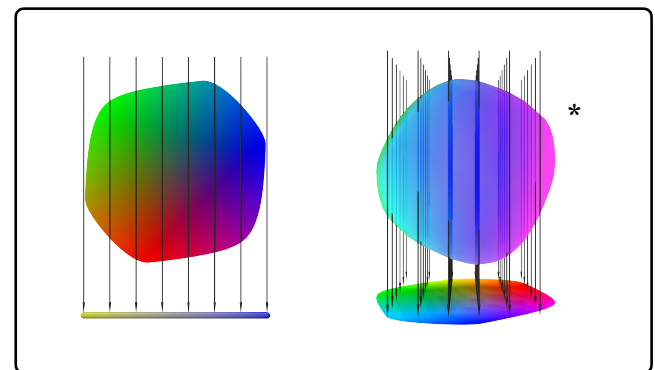


Fig. 7. Color blindness and Comparative Dimensionality of Chromaticity Space. Left: Projection of the trichromatic chromaticity disk onto the dichromatic chromaticity line (protanope). The dichromat confuses colors along the L cone projection lines, resulting in red-green color blindness and an impoverished sense of hue compared to trichromats. Right: the analogous projection of the tetrachromatic chromaticity ball onto the trichromatic chromaticity disk. Similar to before, the trichromat confuses colors along the Q cone projection lines, resulting in a similarly fundamental level of color blindness compared to tetrachromats. Keep in mind (*) that the tetrachromatic hues are visualized here as they would appear to a trichromat and cannot convey to trichromat readers the fact that every point on the surface of the ball is predicted to be a distinct hue to a tetrachromat observer.

green, as shown in Figure 7. When a trichromat looks at the image, they perceive the colors as discordant with reality.

To get a sense of the color experience of a tetrachromat, imagine what it would be like if you were a trichromat in a world built for dichromats. The paint box would lack the colors to paint a rainbow.

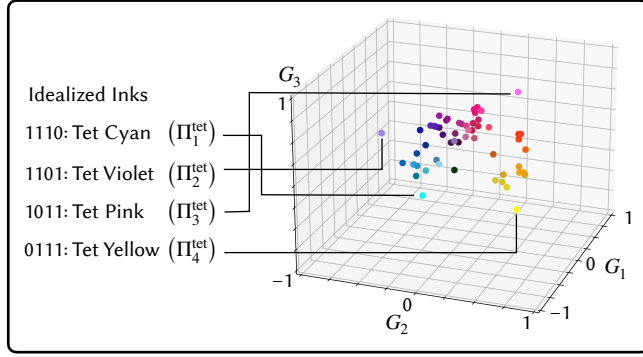


Fig. 8. Library of Fountain Pen Inks. We compiled and spectrally characterized a library of 52 fountain pen inks. The figure plots each ink in tetrachromatic chromaticity space (see 3.3), with each ink plotted as a point with the color that it would appear to a trichromat. Theoretical reference inks are shown for idealized tetrachromatic printing, as described in 3.2.

Many of the hues painted in the world would appear incongruent with reality to you, because the artists were color blind. On the other hand, if the only colors that existed in the world were blue and yellow, if the world was entirely dichromatic, these incongruous colors and lack of rainbows would seem normal to you.

Returning to the case of tetrachromats living in our reality, the defining characteristics of their color experience is living in a world colored entirely by the color blind (trichromats), who have manufactured a world filled with trichromatic colors, but few tetrachromatic colors outside their color blind gamut. In addition, the natural world lacks tetrachromatic colors outside the trichromatic gamut (e.g. projecting hyperspectral images [Arad et al. 2022; Foster et al. 2006; Ruderman et al. 1998] into tetrachromatic colorspace shows that most natural reflectances track the 1D arc of the spectral locus in the 2D hue sphere). Similar to a trichomat living in a dichromatic world, a tetrachromat in our world today may rarely encounter colors that they would view differently to trichromats. If we alter our manufacturing systems to produce colors for tetrachromats, a tetrachromat viewing these colors might have a experience akin to a trichromat living in a dichromatic world and one day seeing a complete set of paints for the first time.

5 PROTOTYPE TETRACHROMATIC PRINTING SYSTEM

5.1 Optimal Ink Theory

For a trichromat, the minimum number of inks to represent the color circle is 3, and the typical three inks chosen are the ink colors Cyan (C), Magenta (M), and Yellow (Y). The reason why these three colors work well is due to their alignment in subtractive mixing. When we mix Cyan and Magenta together, they both reflect everything in the short wavelengths, creating a blue spectra in the ideal case. Each of the combinations MY, CY, and CM, create Red, Green, and Blue, respectively.

An analytical way of finding these relationships, we propose, comes from the inscribed parallelepiped. We argue that the max basis procedure results in the optimal d printing primaries Π , defined in Section 3.2. In topological space, these correspond to the set of d

extremal points that are connected to white. If subtractive mixing is ideal, i.e. mixing inks results in multiplying the reflectances, then the primaries will fill the entire parallelepiped, and therefore fill the gamut optimally for d printing primaries.

For the tetrachromat, we end up with maximal cutpoints at 493nm, 551nm, and 603nm, with the corresponding subtractive ideal primaries denoted as $\Pi_1^{\text{tet}}, \dots, \Pi_4^{\text{tet}}$. These spectra look like Cyan, Violet, Pink, and Yellow so we refer to this basis as CVPY. While they are perceptually similar and share names, the Cyan and Yellow spectra of CVPY are distinct from the spectra in the CMY basis because they absorb less light in the tetrachromatic case. The ideal ink spectra are displayed in Figure 5B connected to the white point. It is important to note that these colors are not simply the chromaticity of the ink, but rather the cutpoints, at which they combine with each other to optimally absorb portions of the spectrum. Knowing that they're equivalent to a two-transition reflectance, it is theoretically possible that the inks may exist, which we explore by spectrally characterizing fountain pen inks.

5.2 Mathematics of Inks and Printer Gamuts

Ideally, we'd have inks that match the ideal CVPY spectra exactly, as that would maximize the gamut coverage for a human tetrachromat. However, most available printer inks are restricted to Cyan, Magenta, and Yellow¹, which have transition points at non-optimal transitions points. Ansari et al. has measured a large library of 40 printer inks, but the inks are fairly similar in hue and do not vary in transition points which would be useful in finding optimal d -dim inks. Therefore, forgoing manufacturing our own printer inks, we expand our ink space to fountain pen inks, since they have more varied color offerings [Ansari et al. 2020]. We therefore model the problem of ink gamut generation as maximizing the coverage of the d -dim object color solid by choosing k inks from a library of $K \gg k$ inks.

In order to simulate the ink gamut, we must sample the reflectances of the k inks in varying combinations and percentages. The Neugebauer equations can be understood as a k -linear interpolation between the binary combinations of the inks. These 2^k binary combinations, known as Neugebauer superpositions, define a k -hypercube, where we want to approximate all the interior values. To account for subsurface scattering on the substrate, a Yule-Nielsen correction term with value η is applied to the linear probabilistic model, yielding the following equation:

$$R(\lambda) = \left(\sum_{i=1}^{2^k} w_i (R_i(\lambda))^{1/\eta} \right)^{\eta}$$

where $R_i(\lambda)$ is the reflectance at a given wavelength λ , and w_i are the multilinear interpolation weights for each superposition i [Balasubramanian 1999]. Previous work has established well-agreed values for η on various substrates, and found that $\eta \rightarrow \infty$ works best for office paper [Hébert 2014].

Since it is intractable to measure all 2^k superpositions for each k -subset for a large ink library, we use the Kubelka-Munk (KM)

¹A black ink is included to save on ink consumption and increase dynamic range of dark regions when combining the CMY inks, but this only nominally expands the printer's achievable color gamut.

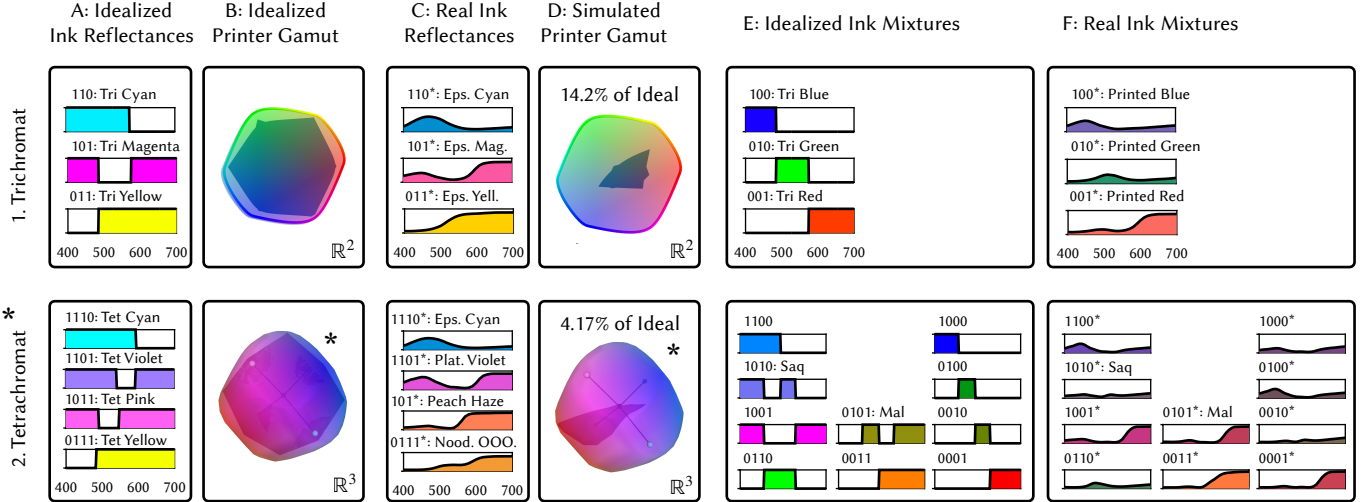


Fig. 9. Comparison of Idealized and Real Printer Inks for Trichromats (Row 1) and Tetrachromats (Row 2). For trichromats, the three required inks for printers are well known to be cyan (C), magenta (M) and yellow (Y). A1 shows our computation of the idealized reflectance functions for C, M and Y, and 1.B shows the resulting printer gamut in the 2D trichromatic chromaticity disk. In C1 and D1, the real trichromatic printer is a consumer Epson EcoTank printer, with measured ink reflectances shown in C1 and simulated gamut shown in D1. Row 2 shows the novel tetrachromatic inksets and gamuts derived in this research. A2 shows reflectance functions for the idealized tetrachromatic ink set computed in 5.1, which would appear cyan (C), violet (V), pink (P) and yellow (Y) to a trichromat. B2 shows the computed idealized gamuts in the 3D tetrachromatic chromaticity ball. C2 shows the reflectance functions for the optimal inks selected from our database of fountain pen inks (see 5.3): Epson Cyan, Platinum Violet, Diamine Peach Haze and Noodler's Orange. D2 shows the computed tetrachromatic chromaticity gamut from these real inks. The fraction of idealized gamut for the trichromatic printer is 14% and the fraction of idealized gamut for the tetrachromatic printer prototype is 4%. On the right, Column E shows all the idealized colored mixtures of inks (Neugebauer primaries). Column F shows spectral measurements of real prints of these ink mixtures. In this Figure, each reflectance is labeled with a bit sequence representing that color in the Optimal Primary Basis; for example, a bit sequence of 1010 represents the tetrachromatic color formed by adding only first and third Optimal Primary Basis colors for tetrachromacy, numbered from short to long wavelengths.

model to simulate Neugebauer superpositions in such a way that we only need a single scan per ink. We use a least-squares KM procedure that relies only on the reflectance data for each pigment [Centore 2014]. After we simulate all 2^k superpositions of k inks via Kubelka-Munk, we can use the Neugebauer equations in order to estimate the set of all possible reflectances, e.g. the k -ink printer gamut. We select which k -ink subset to use based on which ink gamut achieves maximal coverage in the d -dim color space.

Since we want to pick a k ink gamut from a set of K library inks that maximizes the coverage in the d -dim color space, we pick metrics that maximize the number of colors that can be printed. The most intuitive metric is fractional coverage of chromaticity space, which we use to evaluate our gamut. Another metric is optimizing for the width in a cone fundamental R_i in the ink gamut. For example, to print tetrachromatic colors that are the same to trichromats, we can optimize for spread in Q activation.

Finally, we can consider the dimensionality of the ink gamut with respect to the d -dim observer. In order to fabricate a tetrachromatic color experience, we are particularly interested a minimal ink set that has full dimension. In the case of tetrachromacy, we want to find the smallest set of inks that will span four dimensions, which can be calculated by checking that the gamut has nontrivial width along each dimension. In practice, we are also concerned with maximizing the width along each dimension.

5.3 Printer Hardware Setup

There are four inks in the minimal basis to print tetrachromatic colors. This poses a hardware problem, as typical commercial printers only have 3 color channels. Specialty printers with more color channels exist, but are more expensive and difficult to program. We prototyped a tetrachromatic printer composed of two consumer printers that we filled with different ink sets, where the output from the first printer is fed into and printed over by the second. This effectively boosts our maximum number of inks from 3 to 6, which is sufficient for our tetrachromatic printing purposes. We used the Epson EcoTank 3830 printer, which has a tank-based ink-loading mechanism that we filled with any ink we chose from our library, using a syringe.

Since most consumer printers use Cyan, Magenta, and Yellow as their basis inks, we needed to explore other sources of inks in order to properly expand the printer gamut. We collected a set of 52 fountain pen inks, seen in Figure 8, which we found work well with the EcoTank-3830. Our ink library mainly consists of inks that appear Cyan, Violet, Pink, and Yellow, as these are visibly similar to our theoretically ideal inks.

In order to reduce the number of times we had to replace the ink in our printer and avoid an exponential number of measurements, we first measure the spectra of each ink in our library and simulated all possible gamuts using the Kubelka-Munk model and the Neugebauer equations. When an optimal 4-ink set is found, we can load it into

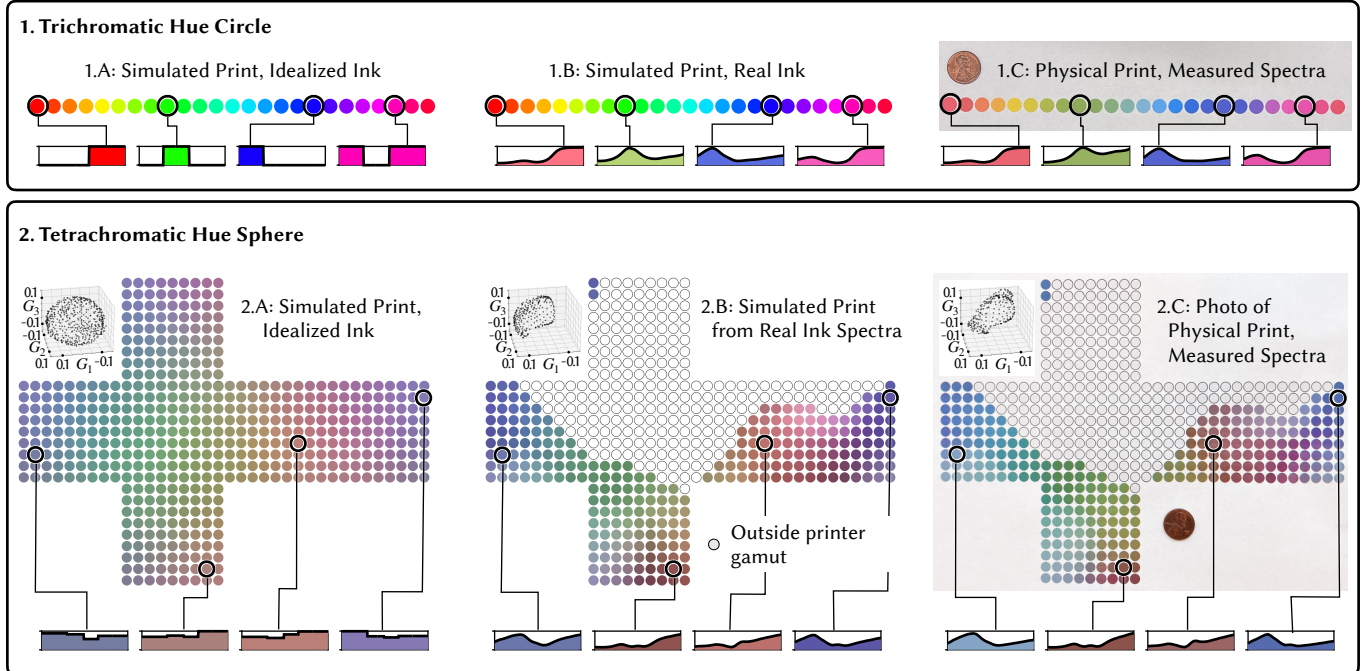


Fig. 10. Simulated and Real Prints Sampling Hue Spaces for Tri- and Tetrachromacy. The prints are a prototype towards fabrication of color vision tests for tetrachromacy that are based on two-dimensional hue ordering (see 3.6). Box 1: first, an example in trichromacy of a linear sampling of the hue circle, with example reflectance functions. 1.A shows a simulated print with the idealized inks for trichromacy shown in Fig. 9-A1. 1.B shows a simulated print using reflectances for real inks shown in Fig. 9-C1. 1.C shows a photograph of a physical print, with spectrally measured reflectance functions as shown. Box 2 shows the analogous examples for the tetrachromatic case, showing a 2D sampling of the hue sphere. The spherical function is visualized here as a flattened cubemap [Greene 1986]. Notice that some dots on the cubemap look visually similar despite being located far apart. This is due to the trichromatic color space this article is printed / displayed in. A functional tetrachromat viewing the original printed cubemap should be able to distinguish these dots. We further show in the left corner of each cubemap the projection of the measured reflectances plotted into tetrachromatic chromaticity space.

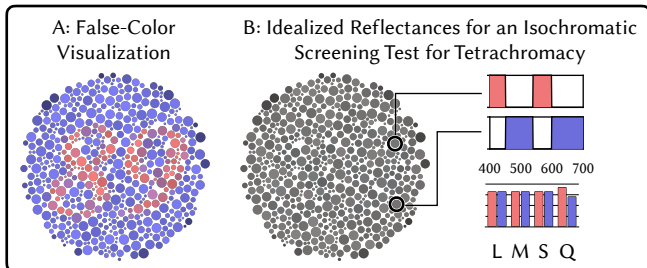


Fig. 11. Idealized Isochromatic Plates for Screening Tetrachromacy. The figure shows the spectral reflectance functions for an image that has a hidden set of digits ('89'), as shown in the false-color visualization. In this example, the foreground and background are the tetrachromatic colors Keef and Litz, respectively, with the shown reflectances. Keef and Litz are metameristic and achromatic for trichromats, causing the same L , M and S , responses, as shown, so the digits appear invisible in a sea of gray dots. However, Keef and Litz are complementary hues of maximum saturation to a tetrachromat, creating a large spread in Q cone response, as shown.

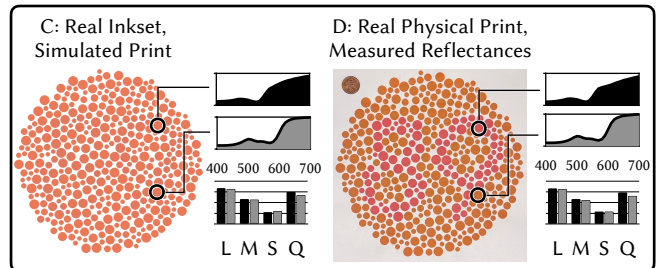


Fig. 12. Prototype of a Real Isochromatic Plate for Screening Tetrachromacy. The figure shows an example of a real, fabricated isochromatic plate with hidden '89' digits similar to those shown in Fig. 11. A: using the real inkset computed in Section 5, we compute the reflectance pair that is metameristic to trichromats with the largest difference in Q activation. These happen to occur at an orange color for this inkset. B: we physically print this tetrachromatic screening test image with our prototype printer. The image shown is a photograph (notice the coin in the frame), and the reflectances are spectrally measured. Note the correspondence between C and D. The latter demonstrate that the real print is indeed metameristic to a trichromat, and would generate a significantly different Q cone response if the Q cone has a spectral peak response at 545 nm.

the printer and directly print the 2^4 Neugebauer superpositions, replacing the KM-derived superpositions with the scanned ones for a more accurate gamut.

5.4 Prototype System Results and Validation

Using both the volume and the Q -axis metrics, we found that the optimal 4-ink gamut basis was Epson brand Cyan, Platinum brand Violet, Diamine brand Peach Haze, and Noodler's Ink brand Operation Overlord Orange [Diamine 2024; Epson 2024; Noodler's Ink 2024; Platinum 2024]. As validation for our set of optimal primaries $\Pi_1^{\text{tet}}, \Pi_2^{\text{tet}}, \Pi_3^{\text{tet}}, \Pi_4^{\text{tet}}$, we see that our found ink set roughly correspond to the cutpoints of the ideal inks of the theoretically maximal basis, as seen in columns A and C of Figure 9.

We can determine the best-case selection of four inks by simulating the ink gamut of the ideal printing primaries $\Pi_1^{\text{tet}}, \Pi_2^{\text{tet}}, \Pi_3^{\text{tet}}$, and Π_4^{tet} . As seen in Figure 9 column B, this ink gamut spans nearly the entire chromaticity space for tetrachromats. Using this volume of this ideal ink gamut in the chromaticity space, we find that our chosen 4-ink set is 4.17% of the ideal volume. We note in column D that Epson cyan, magenta, and yellow inks only span 14.2% of the ideal area for the trichromatic case. In order to determine which tetrachromatic chromaticities our ink set generates, we can use our setup to print tetrachromatic color tests.

5.4.1 4D Color Sphere. In order to demonstrate the span of our ink set in the tetrachromatic gamut, we printed a hue sphere. The radius of our sphere, or the saturation level, was set to 0.15, and the average luminance level was also fixed in sRGB space. We picked the saturation based on the distance from the origin of the FM100 test reflectance [Shen et al. 2022]. We picked the luminance level according to what would print equiluminant points inside of our simulated printer gamut, which we found in practice was a lower luminance than the FM100 values. We then simulated the tetrachromatic hue sphere using ideal inks and our real chosen inks. Some values cannot be printed in the gamut, since the nearest point to the gamut is further than a small ball around the point with a radius of 0.05. We show the hue sphere simulated in ideal ink space, real ink space, and next to it, a real print of the hue sphere in Figure 10. Our printer is able to print $254/486 \approx 52\%$ of the points sampled. This is far more than the CMY gamut alone, which would only fill a rainbow line in the subspace. An example of the spread of this gamut can be on the second and third spectra referenced in Figure 10, which look similar on paper, but have very different ink channel combinations. To show that our printer indeed spans tetrachromatic space, we additionally measured the spectra of each circle printed on the cubemap, and projected the spectra into tetrachromatic chromaticity space (upper left of each cubemap in Figure 10).

5.4.2 Isochromatic Plates. We additionally printed a pseudoisochromatic plate to demonstrate our ability to print tetrachromatic colors. We computed a color pair that was metameristic to the standard human S , M , and L cone types, but distinct to a hypothetical Q cone with a peak halfway between the M and L peaks. At its thickest, the gamut created by our CVPY inks is 29.9% the width of the tetrachromatic object color solid along the Q axis. In comparison, the standard CMY ink gamut is 44% the width of the trichromatic object color solid

along the L axis. Since the CMY gamut is capable of printing the L cone confusion colors required for red-green color blindness tests, this suggests that our printer should be able to print Q cone confusion colors for tetrachromats. For the D65 lighting condition, we found an optimal color pair in *U.S. Web Coated (SWOP) v2* color space at 5% ink resolution to be (05,55,20,95) and (20,05,95,65). These colors produce points in the object color solid of (0.416, 0.29, 0.145, 0.37) and (0.41, 0.28, 0.146, 0.33) in (L, M, S, Q) coordinates, respectively. The simulated and printed isochromatic color plates for these colors is seen in Figure 12. Upon visual inspection, we find that most observers cannot tell the difference between the two prints, however a select few users are able to see the hidden image, which means that the test printed a spectrally distinct confusion color pair.

6 LIMITATIONS AND FUTURE WORK

While our current CVPY printer ink gamut far exceeds CMY in its ability to print tetrachromatic colors, it still only spans half the hue sphere. Our current theory and data indicate that a full human gamut is within reach with real inksets that are closer to the idealized CVPY derived.

This work precedes perceptual validation with known tetrachromatic observers, because few have been confirmed so far in vision science. This paper lays the technical foundation of bringing the most colorful tetrachromat reflectances into physical existence, which supports searching for tetrachromats in the wild, at scale.

The technical development here would benefit significantly from a perceptually-uniform metric of color difference. Our development is limited to linear tetrachromatic colorspace, which we do not expect to have perceptually uniform density, in the same way that trichromatic RGB and CMY colorspaces are not perceptually uniform. What is lacking is the analogue to perceptually-uniform colorspace models such as CIELAB [CIE 2004] and color appearance models [Fairchild 2013] in trichromacy. Creating such nonlinear tetrachromatic colorspaces will require perceptual studies and psychophysical data on human tetrachromats, similar to MacAdam's original work on trichromats that led to the MacAdam ellipses [1942].

Our current fabrication work focuses on creating tetrachromatic colors in the multiplicative color mathematics of printing. Other methods of color reproduction, such as the additive color of emissive color displays, will have their own benefits and downsides. Tetrachromatic displays would not be able to fabricate a large number of standalone tetrachromatic images as printers can, but they have the potential to show more saturated colors and are not limited to static images.

7 CONCLUSION

In this paper, we have laid groundwork for understanding higher dimensional color spaces, and for developing a color management pipeline suited for this new dimension. We extend the computation and analysis of the object color solid, chromaticity space and hue manifold to the case of human tetrachromacy, and analyze its higher dimensional topology to make predictions about the fundamentally different, richer color experience of human tetrachromats. We develop a prototype tetrachromatic printer utilizing a library of

fountain pen inks, and succeed at extending the color gamut into the fourth dimension (with significant room for improvement).

It is hard to imagine color experiences fundamentally different to our own. For example, how can a person with conventional color blindness imagine or understand the trichromat's experience of the colors red and green, or the visual splendor of the rainbow? Similarly, the majority of humans today are centered in a trichromatic color experience. We have built a physical world filled with – and limited to – the rainbow of colors that we can see. How can humans today imagine the novel tetrachromatic experiences of the complementary colors keef and litz, the continuum of neighboring hues that encircle each and every tetrachromatic color, or the full visual complexity of a world of hues that spans a sphere rather than just a circle? In this paper we have shown how d -dimensional color theory reveals clear, detailed predictions about these remarkably different color experiences. But the perceptual qualia of such color experience can only be understood by seeing. This line of research aims to bring such colors into the physical world, and potentially to reveal human tetrachromacy in the wild, at scale.

ACKNOWLEDGMENTS

This work was supported by the Air Force Office of Scientific Research under award numbers FA9550-20-1-0195 and FA9550-21-1-0230. The authors would like to thank James Fong for the two-pass printing idea, and Michael Wang for preliminary research work on this project. The authors are grateful for conversations with Jay Neitz, Bruno Olshausen, Atsunobu Kotani and Alex Belsten.

REFERENCES

- Navid Ansari, Omid Alizadeh-Mousavi, Hans-Peter Seidel, and Vahid Babaei. 2020. Mixed Integer Ink Selection for Spectral Reproduction. *ACM Trans. Graph.* 39, 6, Article 255 (November 2020), 16 pages. <https://dl.acm.org/doi/10.1145/3414685.3417761>
- Boaz Arad, Radu Timofte, Rony Yahel, Nimrod Morag, Amir Bernat, Yuanhao Cai, Jing Lin, Zudi Lin, Haoqian Wang, Yulin Zhang, et al. 2022. Ntire 2022 spectral recovery challenge and data set. In *Proceedings of the IEEE/CVF Conference on Computer Vision and Pattern Recognition*. 863–881.
- Raja Balasubramanian. 1999. Optimization of the spectral Neugebauer model for printer characterization. *Journal of Electronic Imaging* 8, 2 (1999), 156–166.
- JL Barber, M Rodriguez-Carmona, JA Harlow, K Mancuso, J Neitz, and M Neitz. 2008. A study of unusual Rayleigh matches in deutan deficiency. *Visual Neuroscience* 25, 3 (2008), 507–516.
- Jennifer Birch. 1997. Efficiency of the Ishihara test for identifying red-green colour deficiency. *Ophthalmic and Physiological Optics* 17, 5 (1997), 403–408.
- Dietrich Burkhardt. 1989. UV vision: a bird's eye view of feathers. *Journal of Comparative Physiology A* 164, 6 (1989), 787–796.
- Paul Centore. 2013. A Zonohedral Approach to Optimal Colours. *Color Research & Application* 38, 2 (2013), 110–119.
- Paul Centore. 2014. Perceptual Reflectance Weighting for Estimating Kubelka-Munk Coefficients. <https://www.munsellcolorscienceforpainters.com/ColourSciencePapers/PerceptualReflectanceWeightingForKubelkaMunk.pdf>.
- CIE. 2004. *CIE Technical Report, Colorimetry, 3rd Edition*. Commission Internationale de l'Eclairage.
- Christopher R Cooney, Yichen He, Zoë K Varley, Lara O Nouri, Christopher JA Moody, Michael D Jardine, András Liker, Tamás Székely, and Gavin H Thomas. 2022. Latitudinal gradients in avian colourfulness. *Nature Ecology & Evolution* 6, 5 (2022), 622–629.
- Candice Davidoff. 2015. *Cone opsin gene variants in color blindness and other vision disorders*. Ph.D. Dissertation. <https://digital.lib.washington.edu:443/researchworks/handle/1773/33578>
- Candice Davidoff, Maureen Neitz, and Jay Neitz. 2016. Genetic testing as a new standard for clinical diagnosis of color vision deficiencies. *Translational vision science & technology* 5, 5 (2016), 2–2.
- Diamine. 2024. Diamine Peach Haze. <https://www.diamineinks.co.uk>.
- David Eppstein. 1995. Zonohedra and Zonotopes. (1995). <https://ics.uci.edu/~eppstein/junkyard/ukraine/ukraine.html>
- Epson. 2024. Epson 200 Ink. <https://epson.com>.
- Mark D Fairchild. 2013. *Color Appearance Models*. John Wiley & Sons.
- Dean Farnsworth. 1943. The Farnsworth-Munsell 100-hue and dichotomous tests for color vision. *JOSA* 33, 10 (1943), 568–578.
- David H Foster, Kinjirō Amano, Sérgio MC Nascimento, and Michael J Foster. 2006. Frequency of metamerism in natural scenes. *JOSA A* 23, 10 (2006), 2359–2372.
- Timothy H Goldsmith. 1990. Optimization, constraint, and history in the evolution of eyes. *The Quarterly Review of Biology* 65, 3 (1990), 281–322.
- Ned Greene. 1986. Environment Mapping and Other Applications of World Projections. *IEEE Comput. Graph. Appl.* 6, 11 (nov 1986), 21–29. <https://doi.org/10.1109/MCG.1986.276658>
- Mathieu Hébert. 2014. Yule-Nielsen effect in halftone prints: Graphical analysis method and improvement of the Yule-Nielsen transform. *Proc SPIE* 9015, 90150R.
- Shinobu Ishihara et al. 1918. Tests for color blindness. *American Journal of Ophthalmology* 1, 5 (1918), 376.
- Yuhua Jin, Isabel Qamar, Michael Wessely, and Stefanie Mueller. 2020. Photo-Chameleon: Re-Programmable Multi-Color Textures Using Photochromic Dyes. In *ACM SIGGRAPH 2020 Emerging Technologies* (Virtual Event, USA) (SIGGRAPH '20). Association for Computing Machinery, New York, NY, USA, Article 7, 2 pages. <https://doi.org/10.1145/3388534.3407296>
- Gabriele Jordan, Samir S Deeb, Jenny M Boston, and JD Mollon. 2010. The dimensionality of color vision in carriers of anomalous trichromacy. *Journal of Vision* 10, 8 (2010), 12–12.
- Gabriele Jordan and John Mollon. 2019. Tetrachromacy: The mysterious case of extraordinary color vision. *Current Opinion in Behavioral Sciences* 30 (2019), 130–134.
- Jan Koenderink, Andrea van Doorn, and Karl Gegenfurtner. 2021. RGB colors and ecological optics. *Frontiers in Computer Science* 3 (2021), 630370.
- Jan J Koenderink. 2010. *Color for the Sciences*. MIT press.
- Paul Kubelka. 1931. Ein Beitrag zur Optik der Farbanstriche. *Z. Tech. Phys.* 12 (1931), 593–601.
- Alexander D Logvinenko and Vladimir L Levin. 2022. *Foundations of Colour Science: From Colorimetry to Perception*. John Wiley & Sons.
- David L MacAdam. 1935. The Theory of the Maximum Visual Efficiency of Colored Materials. *JOSA* 25, 8 (1935), 249–252.
- David L MacAdam. 1942. Visual sensitivities to color differences in daylight. *JOSA* 32, 5 (1942), 247–274.
- Kelli McCown. 2023. Mountain of ink. <https://mountainofink.com>
- Jay Neitz and Maureen Neitz. 2011. The genetics of normal and defective color vision. *Vision Research* 51, 7 (2011), 633–651.
- Jay Neitz, Maureen Neitz, and Gerald H Jacobs. 1993. More than three different cone pigments among people with normal color vision. *Vision Research* 33, 1 (1993), 117–122.
- Keith K Niall. 2017. *Erwin Schrödinger's Color Theory*. Springer.
- Noodler's Ink. 2024. Noodler's Ink - 19056 V-Mail Operation Overlord. <https://noodlersink.com>.
- W. Ostwald and J.S. Taylor. 1931. *Colour Science: A Handbook for Advanced Students in Schools, Colleges, and the Various Arts, Crafts, and Industries Depending on the Use of Colour*. Winsor & Newton Limited.
- Petar Pjanic and Roger D Hersch. 2015. Color imaging and pattern hiding on a metallic substrate. *ACM Trans. Graph.* 34, 4 (2015), 1–10.
- Platinum. 2024. Platinum Pen USA - Inks & Accessories. <https://platinumpenusa.com/inksaccessories/>
- J. P. Reffin, S. Astell, and J. D. Mollon. 1991. *Trials of a computer-controlled colour vision test that preserves the advantages of pseudoisochromatic plates*. Springer Netherlands, Dordrecht, 69–76. https://doi.org/10.1007/978-94-011-3774-4_9
- Benedict C Regan, JP Reffin, and John D Mollon. 1994. Luminance noise and the rapid determination of discrimination ellipses in colour deficiency. *Vision Research* 34, 10 (1994), 1279–1299.
- Dragos L Rezeanu, James Kuchenbecker, Rachel Barborek, Marcus Mazzaferri, Maureen Neitz, and Jay Neitz. 2021. Explaining the Absence of Functional Tetrachromacy in Females with Four Cone Types. *Investigative Ophthalmology & Visual Science* 62, 8 (2021), 527–527.
- Daniel L Ruderman, Thomas W Cronin, and Chuan-Chin Chiao. 1998. Statistics of cone responses to natural images: implications for visual coding. *JOSA A* 15, 8 (1998), 2036–2045.
- Kaisei Sakurai, Yoshinori Dobashi, Kei Iwasaki, and Tomoyuki Nishita. 2018. Fabricating reflectors for displaying multiple images. *ACM Trans. Graph.* 37, 4 (2018), 1–10.
- Erwin Schrödinger. 1920. Theorie der Pigmente von grösster Leuchtkraft. *Annalen der Physik* 367, 15 (1920), 603–622.
- Che Shen, Robert Wanat, Jang Jin Yoo, Junwoo Jang, and Mark D Fairchild. 2022. Measuring and modeling display observer metamerism. *The Visual Computer* 38, 9–10 (2022), 3301–3310.
- Liang Shi, Vahid Babaei, Changil Kim, Michael Foshey, Yuanming Hu, Pitchaya Sithithamorn, Szymon Rusinkiewicz, and Wojciech Matusik. 2018. Deep Multispectral

- Painting Reproduction via Multi-Layer, Custom-Ink Printing. *ACM Trans. Graph.* 37, 6, Article 271 (November 2018), 15 pages. <https://doi.org/10.1145/3272127.3275057>
- Šárka Sochorová and Ondřej Jamriška. 2021. Practical Pigment Mixing for Digital Painting. *ACM Trans. Graph.* 40, 6, Article 234 (December 2021), 11 pages. <https://dl.acm.org/doi/10.1145/3478513.3480549>
- Givago S. Souza, Felecia L. Malone, Teera L. Crawford, Letícia Miquilini, Railson C. Salomão, Diegol Guimarães, Dora F. Ventura, Malinda E. Fitzgerald, and Luiz Carlos Silveira. 2014. Low number of luminance levels in the luminance noise increases color discrimination thresholds estimated with pseudoisochromatic stimuli. *Frontiers in Psychology* 5 (2014).
- Andrew Stockman and Lindsay T. Sharpe. 2000. The spectral sensitivities of the middle- and long-wavelength-sensitive cones derived from measurements in observers of known genotype. *Vision Research* 40, 13 (2000), 1711–1737. <https://www.sciencedirect.com/science/article/pii/S0042698900000213>
- Andrew Stockman, Lindsay T. Sharpe, and Clemens Fach. 1999. The spectral sensitivity of the human short-wavelength sensitive cones derived from thresholds and color matches. *Vision Research* 39, 17 (1999), 2901–2927.
- Mary Caswell Stoddard, Harold N Eyster, Benedict G Hogan, Dylan H Morris, Edward R Soucy, and David W Inouye. 2020. Wild hummingbirds discriminate nonspectral colors. *Proceedings of the National Academy of Sciences* 117, 26 (2020), 15112–15122.
- Mary Caswell Stoddard and Richard O Prum. 2008. Evolution of avian plumage color in a tetrahedral color space: a phylogenetic analysis of new world buntings. *The American Naturalist* 171, 6 (2008), 755–776.
- Eric J. Stollnitz, Victor Ostromoukhov, and David H. Salesin. 1998. Reproducing color images using custom inks. In *Proceedings of SIGGRAPH 98*. 267–274. <https://doi.org/10.1145/280814.280889>
- Cameron R. Taylor. 2016. Finite Difference Coefficients Calculator. <https://web.media.mit.edu/~crtaylor/calculator.html>.
- Gabriela X Venable, Kaija Gahm, and Richard O Prum. 2022. Hummingbird plumage color diversity exceeds the known gamut of all other birds. *Communications Biology* 5, 1 (2022), 576.
- Thomas Wachtler, Eizaburo Doi, Te-Won Lee, and Terrence J Sejnowski. 2007. Cone selectivity derived from the responses of the retinal cone mosaic to natural scenes. *Journal of Vision* 7, 8 (2007), 6–6.
- Yuh Chang Wei, Wen Min Chou, and Chih Lang Chen. 2011. The Performance of Computerized Spectrum Color Matching Based on Kubelka-Munk Theory and its Color Rendering on Offset Ink Sets. In *Printing and Packaging Study (Advanced Materials Research, Vol. 174)*. Trans Tech Publications Ltd, 72–76.
- Gerhard West and Michael H Brill. 1983. Conditions under which Schrödinger object colors are optimal. *JOSA* 73, 9 (1983), 1223–1225.